Energy & Environmental Science

ROYAL SOCIETY OF CHEMISTRY

PAPER

View Article Online
View Journal | View Issue

Cite this: *Energy Environ. Sci.*, 2022, **15**, 5202

Performance limitations imposed by the TCO heterojunction in high efficiency perovskite solar cells†

Daniel Walter, ‡*[a] Jun Peng, ‡[abc] Klaus Weber, [a] Kylie R. Catchpole [a] and Thomas P. White *[a]

The power conversion efficiency of perovskite solar cells (PSCs) has risen rapidly, but continuing this trend requires a clear view of all possible sources of power loss. Over the past decade in which we have witnessed these remarkable improvements, the transparent conductive oxide (TCO) has been widely treated as an extrinsic element. While it is recognised that the TCO contributes power loss due to finite lateral resistance and optical losses, comparatively little attention has been paid to the influence of the TCO on the electrostatics in other cell layers. However, a recent fill factor (FF) record on a centimetre-scale PSC has refocused attention on how the TCO can play a significant role in the optoelectronic properties across the entire TCO-transport layer-perovskite interface. Primarily, this is the consequence of the Schottky-type heterojunction formed between the TL and TCO layers, which establishes a space-charge region within the TL. Due to the extreme thinness of many TL layers, the space charge region can extend the full width of the TL and even into the perovskite layer itself. In effect, the bulk properties of the TL come to be dominated by the equilibrium conditions of this junction, with the consequence that the TL can be markedly less conductive once *in situ* within a PSC. This *in situ* resistance can significantly reduce FF, but without knowledge of this mechanism, the source of resistance and FF loss would be non-obvious. In this contribution, we employ ionic–electronic device models to quantify the TCO-induced *in situ* conductance of the transport layer and demonstrate its characteristic appearance in the *JV* curves of high-performance PSCs. We posit that widely used titanium dioxide (TiO_2) can be particularly susceptible to a low *in situ* conductance, which explains the years-long plateau of FFs in TiO_2-based PSCs in the low 80%-range. By comparison to inverted PSCs, we illustrate how the TCO influence can explain comparative underperformance of FF relative to open-circuit voltage and photocurrent in state-of-the-art n–i–p PSCs. We hope that by refocusing attention on this factor of PSC design, this work can provide a facile path to plausibly lifting single junction PSCs beyond 26% efficiency.

Received 1st June 2022,
Accepted 24th October 2022

DOI: 10.1039/d2ee01742c

rsc.li/ees

Broader context

Single junction, small area perovskite solar cell (PSC) efficiency now sits at a remarkable 25.7%, close to the record for crystalline silicon at 26.6%, and closing in on the theoretical limit of *circa* 30–31%. Further efficiency gains will be increasingly difficult, motivating a close, careful look at possible sources of power loss in state-of-the-art PSCs. A notable limitation in n–i–p PSCs is fill factor (FF), which has historically lagged improvements in open-circuit voltage and photocurrent. In this work, we draw upon our group's recent FF record >86% to argue that the electrostatics of the transparent conductive oxide (TCO)-transport layer-perovskite interface plays a critical role in determining resistive power losses in the TL, and hence FF. These losses can be much larger than predictions based on TL conductivity alone. Thus, we provide explanations for the generally disappointing fill factors achieved with TiO_2-based PSCs and the high FFs achieved in inverted (p–i–n) PSCs. In doing so, we identify transport layer properties that mitigate this performance limit. Ultimately, we argue that future theoretical and experimental work in PSCs must account for the interactions between all layers of the PSC electrodes to push efficiencies to 26% and beyond.

[a] *School of Engineering, The Australian National University, Canberra, Australian Capital Territory, Australia. E-mail: daniel.walter@anu.edu.au, thomas.white@anu.edu.au*
[b] *Institute of Functional Nano & Soft Materials (FUNSOM), Joint International Research Laboratory of Carbon-Based Functional Materials and Devices, Soochow University, Suzhou, Jiangsu 215123, P. R. China*
[c] *Jiangsu Key Laboratory of Advanced Negative Carbon Technologies, Soochow University, Suzhou, Jiangsu 215123, P. R. China*

† Electronic supplementary information (ESI) available. See DOI: https://doi.org/10.1039/d2ee01742c

‡ Denotes equal contribution.

Introduction

The transparent conductive oxide (TCO) constitutes the sunward-facing electrode of a perovskite solar cell (PSC) in single-junction or tandem configurations and conducts electric charge between the active cell layers and an external circuit. To date, the TCO has been widely treated as a passive cell component that has no direct bearing on charge conductivity within the PSC itself. In theoretical treatments (*i.e.* numerical device simulations) the influence of the TCO is rarely considered. However, a recent result from our group presents strong evidence that the TCO layer, through the heterojunction it forms with the sunward-facing transport layer (TL) can be influential on both the conductivity of the TL and to a lesser extent on non-radiative recombination within the perovskite layer itself. This result was a certified fill factor (FF) of more than 86% (PCE = 23.3%) on a 1 cm^2 n–i–p PSC.[1] This FF was an average improvement of ~6% absolute over a control structure, characterised by a reduction in the series resistance component of the *JV* curve and a small improvement in open circuit voltage (Fig. 1). Remarkably, the control and high-efficiency devices were distinguished by a single structural change: substitution of a solution processed, lowly doped TiO_2 film ($N_D \approx 5 \times 10^{14}$ cm^{-3}) for a heavily doped titanium oxy-nitride (TiO_xN_y) film ($N_D \approx 3 \times 10^{17}$ cm^{-3}) as the electron transport layer (ETL). Characterisation of these ETL materials showed that the only conclusive difference was the *circa* three order-of-magnitude increase in n-type ionized dopant density, with no significant change in other relevant properties such as electron affinity, bandgap, electron mobility and the perovskite crystal structure.[1]

A FF on the order of 86% cannot be achieved unless all other factors of the PSC are highly performant. From this perspective, the lowly-doped, solution-processed TiO_2 ETL was a significant bottleneck to performance. The experimental *JV* characteristics of the TiO_2 and TiO_xN_y cells show that the FF difference is predominantly the result of higher series resistance in the TiO_2-based cell, with negligible changes in open-circuit voltage, short-circuit current density or shunt resistance (Fig. 1). However, Hall effect measurements on the TiO_2 film external to the PSC quantified conductivity at ~10^{-4} S cm^{-1}, for an Ohmic series resistance of ~50 mΩ cm^2 in a 50 nm thick film. At the maximum power point current of approximately 20 mA cm^{-2}, the voltage loss contributed by this resistance is only ~1 mV, while the experimentally observed difference was ~80 mV. Thus, the *ex situ* conductivity cannot explain the restriction placed on FF and PCE, nor the gains realised with TiO_xN_y. Instead, an explanation that is consistent with these observations is the influence of the TCO layer on the electrostatics of the PSC itself, *via* a mechanism referred to in the wider thin-film solar cell literature as a "parasitic Schottky junction" (PSJ).[2–5]

A PSJ is the consequence of the work function difference, $\Delta\varphi$, between the TL and TCO. When in intimate contact, the materials exchange electrons until their Fermi levels are in equilibrium. Given the high dopant density of the TCO, the heterojunction forms an asymmetric space charge region that extends predominantly into the TL. Within the space charge region, majority carriers are depleted up to several orders of magnitude below the nominal density. With typical TL thickness of 50 nm or less, this space charge region can extend the full width of the TL and thus come to completely determine the conductivity of the TL once in place within a PSC. For the following discussion, we define the *ex situ* conductivity as the conductivity of the film outside of the cell, without the influence of the PSJ space charge region. Conversely, we define *in situ* conductivity as the conductivity when the TL is in place within the cell, with bulk properties determined by the electrostatic equilibrium of the perovskite–TL–TCO interface. In Fig. 2, we plot the simulated *ex situ* and *in situ* conductivity of a 50 nm-thick ETL as a function of dopant density, accounting for the influence of the TCO.

The device modelling behind Fig. 2 we will describe in detail in the next section. For now, the key observations are that (1)

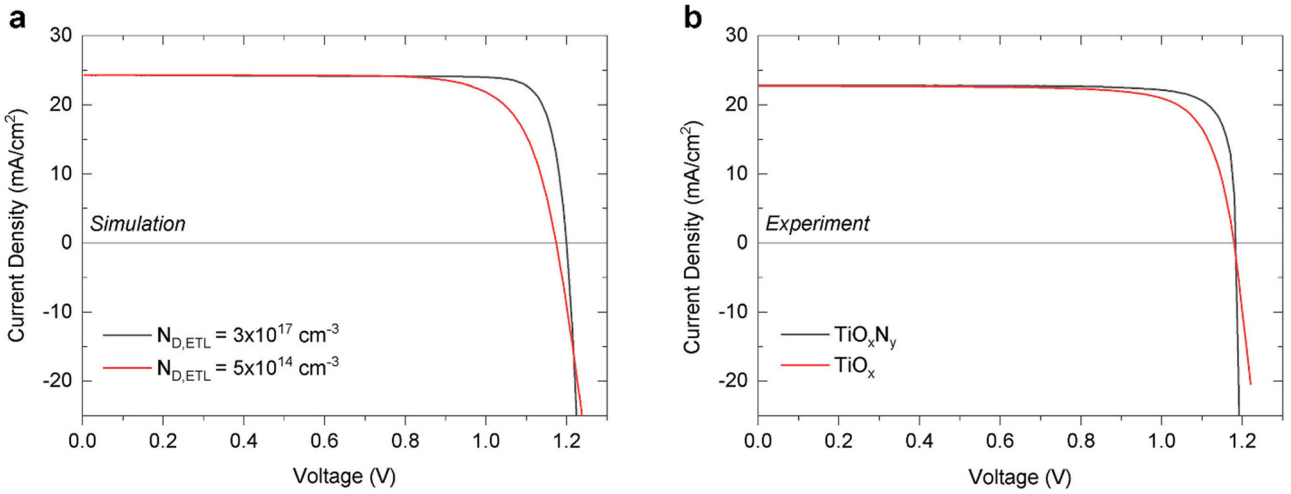

Fig. 1 Comparison between simulated (a) and experimental (b) *JV* curves illustrating the performance improvement following the substitution of TiO_2 for TiO_xN_y In the simulated curves of (a) only ETL doping is varied, taking ionised dopant densities from Hall effect measurements. Reduction in FF and increase in Ohmic series resistance is due to electron depletion in the ETL layer, a consequence of the space charge region of the ETL/TCO heterojunction. Reproduced from ref. 1.

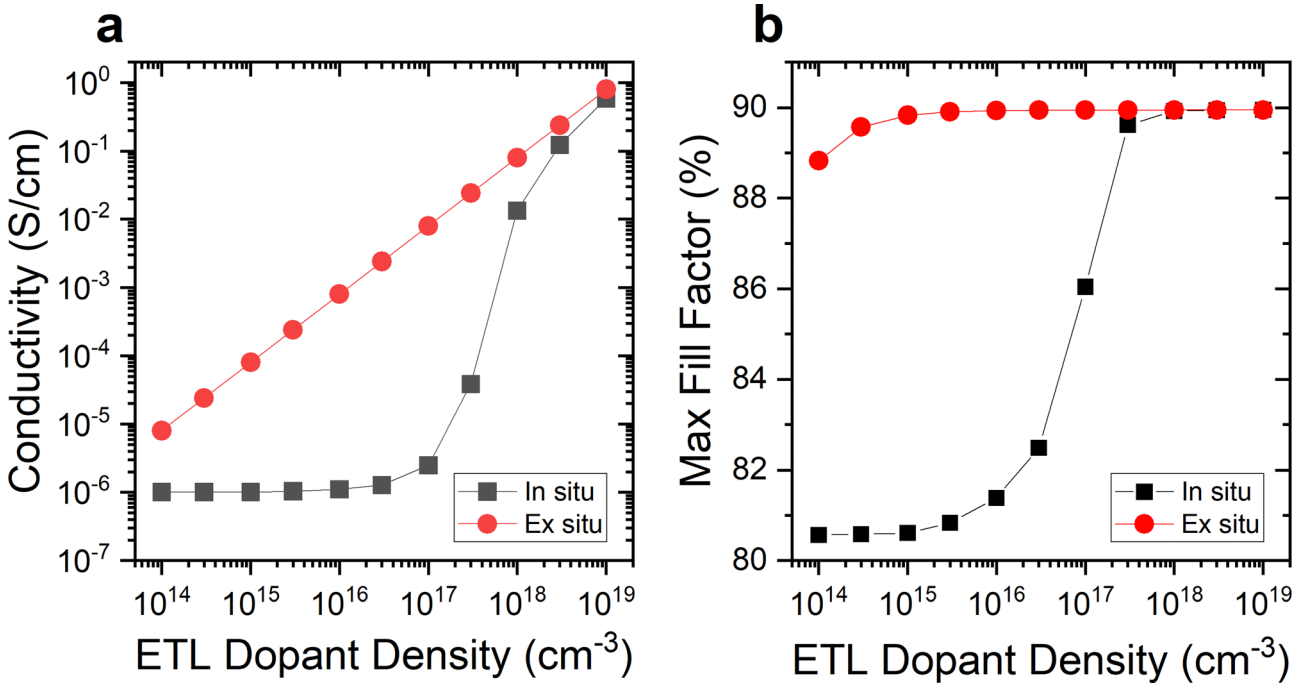

Fig. 2 (a) *Ex situ* conductivity, calculated based on nominal doping density, and *in situ* conductivity calculated from the equilibrium carrier density at the maximum power point for each cell. At worst, the *in situ* conductivity is almost four orders of magnitude below the *ex situ* value. (b) Taking the *in situ* conductivity calculated in (a), the theoretical maximum fill factor for a 50 nm thick ETL with an electron mobility of 0.5 $cm^2\ V^{-1}\ s^{-1}$ compared to a device where the *ex situ* conductivity is maintained once the ETL is in place in the PSC.

for all TL dopant densities (N_D) conductivity is reduced by the space charge region of the TL/TCO heterojunction, and (2) at lower values of N_D, which for the set of parameters in this example is $\lesssim 10^{17}$ cm^{-3}, conductivity is pinned at a very low level. This has two consequences. Firstly, if the *ex situ* conductivity of the TL is only marginally sufficient for a high FF solar cell, even a heavily doped transport layer ($N_D \gtrsim 10^{17}$ cm^{-3}) may be sufficiently depleted to have a measurable impact on FF. This would occur along the range of dopant densities for which the *in situ* conductivity decreases rapidly as illustrated in Fig. 2b. Secondly, at low N_D, the resistance of the TL once in intimate contact with the TCO can place an upper limit on FF. To compute this limit, we used an idealised one-diode equivalent circuit model, which presumes there are no other sources of (non-ideal) power loss in the cell. This computes an upper limit of FF of $\lesssim$83% (Fig. 2b). In other words, the *in situ* conductance of the 50 nm-thick TL is on its own sufficient to reduce FF by ~7%, corresponding to an absolute efficiency loss of ~2%. Critically, the cause would not be obvious based on *ex situ* measurements of the TL conductivity, which would suggest negligible resistance losses.

The influence of the Schottky junction, also referred to as the Schottky barrier, is a known loss mechanism in thin film solar cells and in the last two decades has received attention in the thin film and silicon heterojunction PV literature. Often, this work has focused on the impact of the energy barrier to charge transport, an energy penalty that must be surmounted for charge to flow, with a characteristic 'S-shape' to the *JV* curve. For example, in 2006 the TL/TCO Schottky barrier was called upon by Snaith and Grätzel to explain a low FF, S-shaped *JV* curve under monochromatic illumination in a dye-sensitized solar cell.[3] In an early 2014 review, Green *et al.* computed an energy band diagram of a complete PSC, identifying an energy barrier to electron flow at the TiO_2/FTO interface. However, it was suggested that the absence of obvious characteristics of an energy barrier indicated a smaller barrier in practice than predicted by idealised theory.[6] Motivated by the observations of Snaith and Grätzel, one of the first PSC efficiency milestones from Zhou *et al.* in 2014[7] explicitly aimed to reduce the energy barrier with an ITO surface treatment prior to depositing TiO_2. In 2014, Wojciechowski *et al.* proposed a low temperature fabrication process that maximised TiO_2 doping, again with the intention of addressing *in situ* resistance.[8] In 2015, Chen *et al.*[9] doped a TiO_2 layer with Nb to achieve a then record efficiency of 16.2%, recognising also the advantages for minimising PSJ losses. Beyond perovskite photovoltaics, simulations of the TCO heterojunctions in silicon heterojunction solar cells by Zhao *et al.*[5] and Bivour *et al.*[4] demonstrated that the space charge region of the TL/TCO structure could be detrimental to PCE *via* a reduction in FF.

Yet despite early attention in the PSC literature, in the years that followed only a small number of works explicitly referenced the PSJ and engineered PSC architectures to minimise associated losses.[1,10–12] Furthermore, the theory of charge conduction in PSCs, exemplified by numerical device modelling, has almost completely ignored the TCO.[13–16] One exception is a study from Sherkar *et al*, who observed a fill factor dependence on the energy barrier at the TL/TCO interface, but beyond the

importance of the TL/TCO work function difference, did not consider the impact on bulk conductivity of the TL and how it may be mitigated.[12] The fact that the impact of the PSJ in PSCs has hitherto not been rigorously quantified and characterised may explain why the phenomenon has faded from view, demonstrated by recent record PCEs that approach and exceed 25% but make no mention of this mechanism or explicitly attempt to address it.[17–19]

We develop a quantitative understanding of the PSJ in PSCs in the following section. One key observation from our analysis of the PSJ—which to our knowledge has not been quantified before in the perovskite literature—is the added influence the TCO can have on electrostatics and recombination within the perovskite layer itself. Where the TL contains insufficient space charge to fully screen the work function of the TCO, the accumulation of electric charge at the near-interface region of the perovskite is influenced by the TCO work function. Several theoretical studies, including our own, have shown that altering the distribution of ionic charge, and concurrently the distribution of electrons and holes, can influence rates of non-radiative recombination, which ultimately explains many manifestations of hysteresis in PSCs.[13,15,20,21] In our theoretical exploration of the TCO's influence, we observed that the greater the influence of the TCO on the perovskite layer, the higher the rate of nonradiative recombination at any given defect density due to increased accumulation of minority charge carriers at the TL–TCO interface. This was consistent with our experimental observations in the substitution between TiO_2 and TiO_xN_y,[1] which showed an $\sim$8 mV increase in open circuit voltage. However, the magnitude of this voltage loss is conditional on the perovskite layer's ionic, dopant and recombination-active trap properties. Furthermore, this effect is diminished *via* bulk and interface passivation, while the TL conductivity loss is not. As a result, in this work we focus on the *in situ* conductivity losses. This is because the *in situ* resistance is particularly relevant for the highest performance cells to date, the performance of which suggests strong suppression of non-radiative recombination, exemplified by a recent 24.6% PCE with an open circuit voltage to band gap deficit of $\sim$300 mV described by Jeong *et al.*[17] Nonetheless, the TCO work function can exacerbate non-radiative recombination in PSCs, and thus should be routinely included in device theory and modelling going forward, especially as TLs become increasingly thin and thus less able to screen the TCO from the perovskite layer.

Finally, PSJ theory suggests that the use of TiO_2 transport layers in n–i–p cells may fundamentally limit FF in otherwise ideal PSCs. This is not the consequence of intrinsically low conductivity in TiO_2. Early analysis of TiO_2 films suggested that their amorphous structure severely limited conductivity, to levels as low as 10^{-8} S cm^{-1}.[9] However, higher conductivities, in the range of 10^{-6}–10^{-4} S cm^{-1} are now regularly reported in TiO_2 films with and without additives.[7–9,22–27] According to the idealised calculations using equivalent circuit modelling (Fig. S1, ESI†), conductivity $> 3 \times 10^{-6}$ S cm^{-1} predicts negligible series-resistance losses in 50 nm-thick layers. This then begs the question as to why the highest certified FF on solution-processed or spray pyrolysis TiO_2 is still only 81.8% as recently reported by Jeong *et al.*,[19] despite significant optimisations in all other aspects of the PSC structure. Indeed, breakthroughs in certified FF have only occurred in n–i–p PSC structures following the move away from TiO_2 ETLs. From the perspective of PSJ theory this may be the consequence of a low intrinsic ionised dopant density ($<10^{16}$ cm^{-3}) in some TiO_2 layers, as suggested by several studies,[10,24,26,28] for which electron depletion due to the PSJ will be enough to reduce *in situ* conductivity by several orders of magnitude (Fig. 2). Continued use of such TiO_2 films would then require thicknesses <20 nm to ensure negligible FF losses, which can be challenging to achieve with high conformality.

This study therefore emphasizes that by ignoring the electrostatics of the TL/TCO structure, relatively facile efficiency gains—primarily through reduced series resistance and improved FF—may be going unrealised even in state-of-the-art PSC devices. In addition, where structural changes may have mitigated the PSJ to some extent this factor is not recognised, which may lead to misdirected efforts in optimisation. In the following sections, we begin by describing the physics of the PSJ, its characteristic manifestation in the current–voltage (*JV*) curves of PSCs, and the key material properties that influence the magnitude of the *in situ* conductance. With reference to original numerical, electronic–ionic device simulations and treatments elsewhere in the thin-film solar cell literature, we discuss relatively straight-forward methods for mitigating PSJ power loss. Subsequently, we consider three groups of experimental data that suggest that PSJ losses may be more prevalent than is fully appreciated: (1) the correlation between ETL material and certified FF records in n–i–p PSCs, (2) a direct comparison between two recent certified small area device records $\sim$25%, and (3) evidence of ETL depletion from cross-sectional KPFM profiles. To broaden the scope of our analysis, we will conclude by discussing the implications of the PSJ for *inverted* PSC structures, for which the HTL is the sunward transport layer in contact with the TCO. We consider the extent to which this may explain the generally higher FFs reported on these structures coupled with low open circuit voltages. Ultimately, we make the case that minimising *in situ* resistance due to the PSJ will be essential to raise single junction PCEs beyond 26%.

Physics of the TL–TCO heterojunction

The influence of mobile ionic defects and hysteresis

The simulations of this work were performed in COMSOL Multiphysics, which simulate all device layers in bulk, including the TCO, using an ionic–electronic semiconductor drift diffusion model as previously described.[15,20] These simulations include two mobile ions (anions and cations) of equal concentration. The *JV* simulations are transient in the reverse direction, with a voltage scan rate of 0.1 mV s^{-1}, chosen to reflect a quasi-steady state (QSS) measurement protocol in which the ions are at steady state at each point in the *JV* curve. This avoids the influence of *JV* hysteresis on FF but does capture the influence of the

rearrangement of the mobile ion population as the cell moves along the *JV* curve. In addition, it reflects both the standardized QSS measurement protocol for PSC certification, and practical operating conditions, which stabilize about the maximum power point.

We observed that ion concentration in the perovskite absorber had a small influence on PSJ loss in the ETL and the resultant FF, relative to key factors such as ETL dopant density, and the TL/TCO work function difference as we will describe in the next section. The influence of ion concentration and ETL dopant density on FF is presented in the contour plot of Fig. S2 (ESI†). A greater ion concentration ($>10^{17}$ cm^{-3}) can improve FF by up to approx. 2–3% abs. at any given ETL dopant density. However, in the same device, an increase in ETL dopant density, which reduces PSJ losses, can increase FF by up to 12% abs. at any given mobile ion concentration. Any practical quantity of mobile ions is thus unable to explain, or fully recover, the FF losses due to the PSJ.

Beyond the influence of ions on PSJ FF losses, the rate of non-radiative recombination in a PSC is affected by ion migration in the perovskite absorber.[13,14,20] In effect, recombination 'sensitizes' the *JV* characteristics to the movement of ions during the *JV* scan (among other measurements). However, our device simulations set a low concentration of non-radiative recombination active defects in the perovskite bulk and at the perovskite-transport layer interfaces in order to simulate a high-performance PSC (*i.e.* $V_{oc} \approx 1.24$ V with perovskite bandgap of 1.60 eV). Therefore, our simulations do not predict FF loss due to the influence of ion migration on non-radiative recombination. Instead, our simulations represent high performance, low-hysteresis PSCs and isolate the impact of the PSJ on an otherwise near-lossless device. Given these factors, the following analysis does not consider the influence of mobile ions further, and all simulations use a consistent ion concentration.

The electrostatics of the TL–TCO heterojunction

An *in situ* reduction in TL conductivity induced by the parasitic Schottky junction (PSJ) is driven foremost by the work function difference between the TL and the TCO, $\Delta\varphi$. For this discussion we refer to the resistivity introduced by the space charge region of the PSJ as the *in situ* resistivity (ISR). For clarity, and for its relevance to our analysis of the efficacy of TiO_2 as an electron transport layer (ETL) we will focus on a ''standard'' n–i–p perovskite/ETL/TCO structure and will return to inverted structures later.

In a standard structure, the TCO and the ETL form a heterojunction due to the difference in their work functions, $\Delta\varphi$. The magnitude of $\Delta\varphi$ depends on the TL–TCO materials and the chemistry of the interface formed between them. Although a function of the dopant density, TiO_2 ETLs have work functions on the order of 4.0–4.4 eV,[9,29–31] and for SnO_2 approximately 4.5 eV,[32,33] while fluorine-doped tin oxide (FTO) and indium-doped tin oxide (ITO) materials have work functions that span the range of 4.4–4.8 eV.[34,35] Consequently, we can expect $\Delta\varphi$ to range up to 800 meV, although the plausible range is constrained by practical requirements for effective charge transport. As we will see, magnitudes of $\Delta\varphi < 250$ mV can be sufficient to introduce significant ISR. If the TCO work function exceeds that of the ETL, electrons flow from the ETL to the TCO to reach equilibrium, depleting majority charge carriers within the space-charge region of the ETL. In a Schottky-type heterojunction, the high electron density of the TCO means that it cannot sustain net charge in its bulk, resulting in an asymmetric junction in which the space charge falls entirely on the ETL side. Under many configurations of the junction, the space charge region will extend the full width of the ETL. The thickness of this region in the ETL, w, is approximated by

$$w \cong \sqrt{\frac{2\varepsilon\Delta\varphi}{qN_D}}$$

The width of the space-charge region (and hence total depletion) is proportional to $\Delta\varphi^{1/2}$, and inversely proportional to square root of the ETL dopant density, N_D. Thus, reducing $\Delta\varphi$ or increasing N_D can reduce the magnitude of electron depletion and the ISR. To understand the targets of these parameters in practice, we simulated *JV* curves using an ionic–electronic device model that incorporates all layers of the PSC, including the TCO, for a range of values of $\Delta\varphi$, from 0 to 360 meV (as defined for an ETL work function where $N_{D,ETL} = 10^{17}$ cm^{-3}) for a 50 nm-thick ETL (Fig. 3a). These simulations illustrate both the change in FF and, as importantly, the characteristic appearance of the *JV* curves.

At a fixed ETL dopant density, as $\Delta\varphi$ increases from zero (and w expands), the series resistance component of the *JV* curve increases, and FF and PCE decrease. Then, above a threshold value, which in this example is approximately $\Delta\varphi$ = 250 meV, the energy barrier at the TL/TCO interface is sufficient to introduce a clear s-shape to the *JV* curve. Clearly, we do not see s-shaped curves in well-performing devices. However, the critical observation is that below the ''s-shape threshold'' there is an intermediate range of $\Delta\varphi$ where the *JV* curves simply exhibit non-zero levels of series resistance, but there is no direct evidence that ISR losses are responsible. Suboptimal TCO/ITO junction properties are therefore not a binary condition, revealed by the presence or absence of an S-shaped *JV* curve. That ISR losses can occur in this manner may explain why focus on the PSJ has faded in recent years. There are, after all, many possible sources of series resistance in a solar cell.

Because we are interested in cells with resistance losses within the intermediate range below the s-shape threshold, we now take a closer look at a cell in which $\Delta\varphi$ = 220 meV (blue curve, Fig. 3a). To illustrate how increasing N_D mitigates ISR in the TL, we plot simulated *JV* curves for a range of N_D in Fig. 3b, holding TCO work function constant. The quasi-steady state electron density at the maximum power point of these curves is presented in Fig. 3c. The corresponding equilibrium electric potential profiles, or the relative position of the electron Fermi level, are plotted in Fig. 3d. The relevance of the latter data will

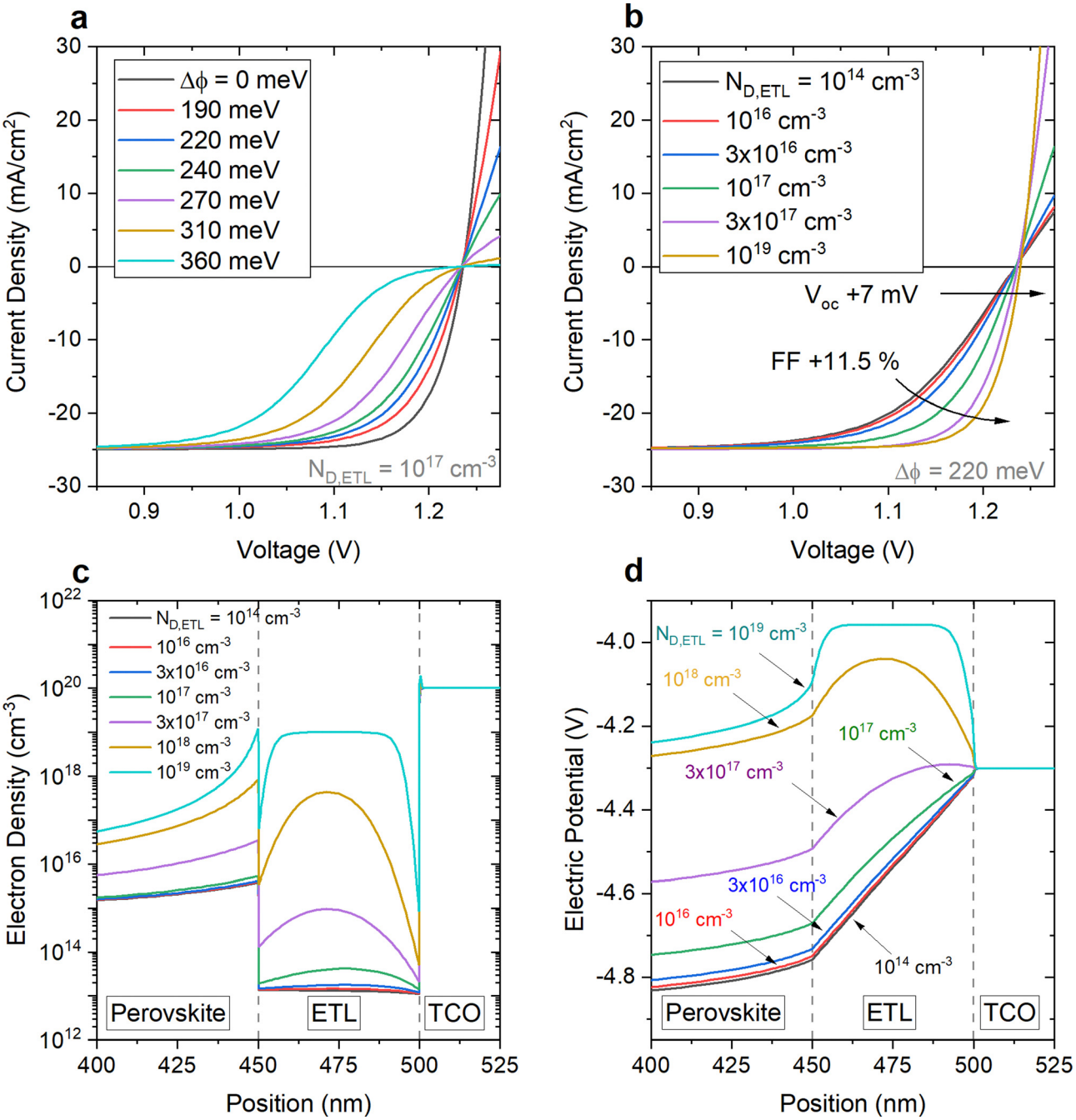

Fig. 3 (a) Simulated *JV* curves as a function of the work function difference between the ETL and ITO layers, $\Delta\varphi$, where $N_{D,ETL} = 10^{17}$ cm^{-3}. (b) Simulated *JV* curves as a function of ETL doping when $\Delta\varphi$ = 220 meV (defined when $N_{D,ETL} = 10^{17}$ cm^{-3}). Heavier doping mitigates against electron depletion from the ETL, recovering both voltage and FF. Note truncated *x*-axis range in (a) and (b), to emphasize differences in the *JV* curves. (c) Simulated electron density as a function of ETL doping at the maximum power point of the *JV* curves plotted in (b). Dashed lines show nominal electron density based on ETL dopant density/conductivities calculated from these profiles are presented in Fig. 2a. (d) Simulated electric potential profile across the ETL layer as a function of ETL doping under semiconductor equilibrium conditions, *i.e.* without illumination or applied bias.

be revealed when we consider experimental contact potential difference profiles as evidence of ISR in the next section.

As shown in Fig. 3b and c, N_D is a critical factor because it determines the density of ionized dopant defects, which constitute the space charge that screens the ETL bulk (and ultimately, the perovskite) from the work function of the TCO. For $\Delta\varphi$ = 220 meV, it is only when $N_D = 10^{19}$ cm^{-3} that there is sufficient space charge density in the ETL to completely screen the ETL bulk from the TCO, such that the ETL bulk carrier density is unchanged from the nominal value. We note that as N_D increases, the Fermi level in the TL rises toward the conduction band minimum, which will increase $\Delta\varphi$. However, our simulations demonstrate that the net change in conductivity is positive with increasing doping. That is, within a limited

range of $\Delta\varphi$, the increased TL/TCO energy barrier from increasing N_D does not introduce significant resistance to electron flow.

Below $N_D = 10^{19}$ cm^{-3}, the space charge region extends deeper into the TL and the magnitude of electron depletion increases. In this example, for $N_D > 10^{17}$ cm^{-3}, although the free electron density falls below N_D, there is still sufficient equilibrium concentration that ISR losses are small, and FF reductions modest. Below 10^{17} cm^{-3}, however, the low equilibrium electron concentration reduces fill factor significantly, as illustrated in Fig. 2. The ISR thus introduces a disproportionately large performance penalty on ETL materials with low dopant density for any given value of $\Delta\varphi$. The aggregate effect on PCE is captured in Fig. 3b. Electron depletion substantially increases resistance in the ETL and as previously observed, increases rates of non-radiative recombination in the perovskite layer by altering charge accumulation at the perovskite/TL interface. The sum of these effects predicts that across an ETL dopant density of 10^{14} to 10^{19} cm^{-3} FF and PCE can rise by up to approx. 11.5% and 3% absolute, respectively. Although the *ex situ* conductivity of the TL predicts a small contribution to series resistance, the ISR can lead to a 'hidden' source of FF loss that only manifests once the ETL is integrated into the device.

As per the preceding discussion, there are three clear approaches to mitigating ISR: (1) reduce $\Delta\varphi$, (2) increase ETL dopant density, (3) reduce ETL thickness or (4) employ ETL materials with high mobility. The work function difference, $\Delta\varphi$, may be the most difficult to control. The energy barrier that forms in practice between two materials is often determined by interface states that are a product of the two materials and the method of preparation, and are difficult to predict or control *a priori*.[36] Nonetheless, transport layer materials with work functions that are closer to that of ITO or FTO are more likely to exhibit smaller work function differences. As we will discuss in more detail in the next section, this favours for example SnO_2 as an ETL material, relatively to TiO_2. On the other hand, TCO materials with shallower work functions could reduce $\Delta\varphi$. One example is Zr-Doped Indium Oxide (IZRO), with a reported work function of 4.2 eV.[37]

Increasing dopant density will also maintain lower ISR for any given value of $\Delta\varphi$, and high doping density TL materials with suitable band alignment vis-à-vis the perovskite absorber, such as SnO_2 and TiO_xN_y, have already been demonstrated in the literature.[28,38] As evidence for the efficacy of increasing N_D in silicon heterojunction solar cells, Bivour *et al.* found that increased boron doping of a p-type amorphous silicon transport layer improved FF up to 4% absolute.[4] ISR losses have not received ongoing attention in silicon heterojunction photovoltaics, which may be explained by the naturally heavy doping of amorphous and poly silicon, which is typically at the solid solubility limit $\gtrsim 10^{20}$ cm^{-3}.[39]

Reducing thickness of the TL will reduce the total resistance for any given conductivity, hence mitigating FF losses. The idealised equivalent circuit simulations of Fig. S1 (ESI†) show that for an ETL layer with an *in situ* conductivity of 10^{-6} S cm^{-1}, reducing thickness from 50 nm to 20 nm improves the FF potential of the cell from ~81% to ~87%, for a gain of approximately 2% (abs) per 10 nm reduction in thickness. However, it is challenging to reduce thickness in solution-processed films such as TiO_2 while avoiding pinholes that increase interface recombination and introduce shunts *via* direct contact between the perovskite and TCO layer.[40] This may favour materials or methods of deposition that can produce conformal coverage at very low thicknesses. Furthermore, if using lowly doped ETLs and attempting to mitigate series resistance *via* a thinner layer, control of thickness will be critical. As previously observed, every 10 nm increase in thickness reduces FF by 2% abs. or PCE by approx. 0.6% abs. This will reduce the degrees of freedom in cell fabrication and may challenge high-throughput industrial manufacturing. By comparison, these fine tolerances will not be present for more heavily doped TLs. Nonetheless, the proven track record of stability and easy integration of TiO_2 films into high efficiency PSCs suggests that deposition methods suitable for sub-20 nm thick films may be worth pursuing.

A sufficiently large majority carrier mobility can also overcome low ISR. Our previous simulations used an ETL electron mobility of 0.5 cm^2 V^{-1} s^{-1}, within the typical range quoted for TiO_2[41] and equivalent to that measured in our TiO_2 and TiO_xN_y films. Yet, as the critical property is the total *in situ* resistance of the transport layer, a larger majority carrier mobility will reduce the ISR for any given magnitude of TL depletion. As an example, in Fig. S3 (ESI†) we plot the achievable fill factor as a function of ETL dopant density and mobility using the idealised equivalent circuit model of Fig. S1 (ESI†) ($\Delta\varphi$ = 220 meV). An ETL mobility >3 cm^2 V^{-1} s^{-1} results in an upper bound on FF of at least 88%—all other factors being equal—relative to approx. 80.5% for a mobility of 0.5 cm^2 V^{-1} s^{-1}. However, the reduction in ISR due to higher mobility can be partially undone by an increase in $\Delta\varphi$, which results in a lower equilibrium electron density (*i.e.* greater depletion). To quantify this effect, Fig. S4 (ESI†) plots the *JV* curves and corresponding fill factor for a device in which the ETL electron mobilities are 3 and 100 cm^2 V^{-1} s^{-1} and $N_{D,ETL} = 10^{17}$ cm^{-3}. The latter mobility is at the upper end of values measured for PSC-compatible ETL materials.[42] Yet even in this case, an increase in $\Delta\varphi$ to 320 meV (the approximate threshold at which an s-shape characteristic appears in the *JV* curve) still produces a fill factor loss of approx. 4% abs. A higher mobility reduces ISR FF loss but does not eliminate the possibility entirely. The broader interdependence of $\Delta\varphi$ and ETL mobility on FF is captured in the contour plot of Fig. S5 (ESI†), which illustrates how larger values of $\Delta\varphi$ can partially reverse the FF gains of higher ETL mobility. Nonetheless, higher transport layer majority carrier mobility is desirable under any circumstances, which favours ETL materials such as ZnO and SnO_2, as we will discuss in the next section.

To conclude this discussion of the PSJ, we consider the other side of the interface: the perovskite–ETL junction. At this interface a heterojunction is formed that can also deplete majority carriers from the ETL. This is a result of the (quasi-)-Fermi level for electrons being below that of the ETL, particularly if the perovskite is p-type. In our simulations, we found that electron depletion in the perovskite layer had a smaller impact, relative to the work function difference with the TCO.

The impact of the ETL-perovskite heterojunction alone is implicitly demonstrated in the simulated *JV* curve for $\Delta\varphi$ = 0 meV (black curve) in Fig. 3a. This magnitude of $\Delta\varphi$ results in negligible electron depletion from the ETL to the TCO, and total FF is predicted to be ~88%. However, the relative magnitude of these losses is conditional on the perovskite properties, *e.g.* fixed dopant density, ion concentration, band gap and electron affinity. It is also impacted by the injection level within the perovskite, which determines the quasi-Fermi level for electrons, the exploration of which are beyond the scope of this study.

Evidence for ISR power loss

In the preceding section, we laid out the theoretical basis for the parasitic Schottky junction (PSJ) in a perovskite solar cell. We identified an intermediate range of PSJ-induced TL depletion that increases series resistance and reduces FF without the characteristic s-shaped *JV* curve that is symptomatic of high energy barriers to charge carrier flow. Now, we consider evidence from the literature, both direct and circumstantial, that ETL depletion may be occurring in even state-of-the-art n–i–p PSC structures.

Power losses due to ISR may be apparent in the historical trend in certified FFs from state-of-the-art PSCs. In Fig. 6, we plot the FF taken from both certified efficiency records reported in the solar cell efficiency tables and other notable certified *JV* measurements, all of which were recorded on an n–i–p structure.[43] Between 2017 and 2019 FF plateaued at approximately 80%, even as open circuit voltage continued to improve. After 2019, FF increased stepwise by roughly 4% absolute and has continued to improve by over 6% absolute with our result in late 2021[28] (Fig. 4). Clearly, there are many structural and compositional differences between these cells. However, one change correlated with the step change in FF is a shift from TiO_2 to tin oxide (SnO_2) and eventually TiO_xN_y, as the ETL material. This invites the question as to whether the improvement in FF from TiO_2 to SnO_2 is due to the same reduction in ISR we observed with the TiO_2 to TiO_xN_y substitution. Measurements of TiO_2 $N_D < 10^{16}$ cm^{-3} [1,10,26,44] could make TiO_2 highly susceptible to ISR, limiting FF to the low 80 s in otherwise high-performance cells (Fig. 2). This is consistent with the plateau in certified fill factors around 80%. Indeed, if we consider progress in TiO_2-based PSCs since 2019, certified FFs have still only reached 81.8%, in this case in a device that currently matches

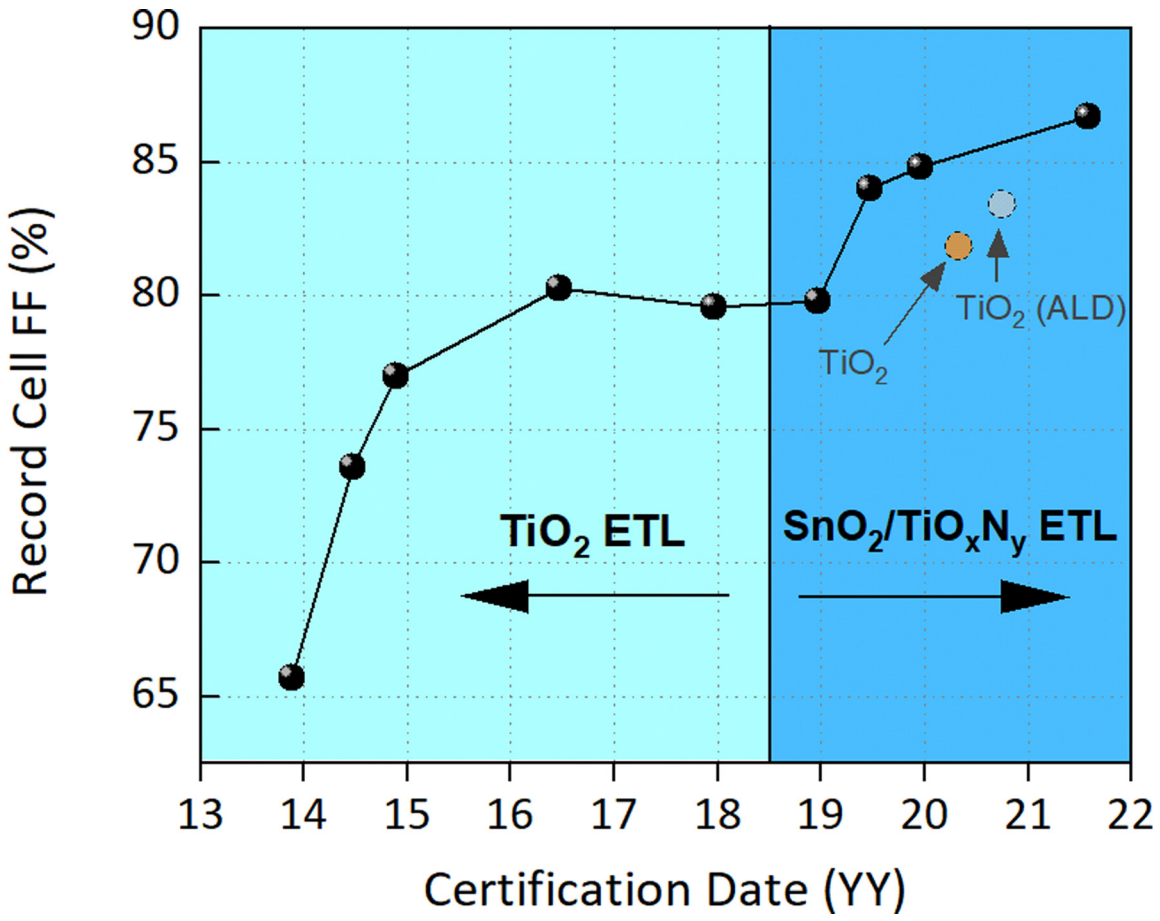

Fig. 4 (a) Certified FFs taken from efficiency tables and other notable certified results, published according to the date of certification.[18,75–79] All cells are n–i–p structures, and the transition from TiO_2 to SnO_2 and TiO_xN_y ETL materials coincides with a step-change increase in FF. The certified result from ANU, plotted independently, was fabricated on ALD TiO_2, for which we have measured doping levels in the range of 10^{17}–10^{19} cm^{-3}.[54] Also plotted is the current certified record FF for a PSC fabricated on non-ALD TiO_2.[19]

the world record in certified PCE of 25.2%,[19] indicative of extremely high performance in all other factors of the cell.

From the perspective of ISR, SnO_2 offers several advantages over TiO_2. Foremost, measured dopant densities, with and without additives, are consistently in the range of 10^{17} to 10^{18} cm^{-3},[27,45,46] of a similar magnitude to TiO_xN_y. In addition, SnO_2 is often deposited at thicknesses $\lesssim$30 nm[45–47] and electron mobility is reported to be as high as $\sim$200–400 cm^2 V^{-1} s^{-1}.[48,49] The larger work function of SnO_2 also reduces the possible magnitude of $\Delta\varphi$. Thus, in minimising ISR, SnO_2 is advantaged along several dimensions: heavier doping results in a higher *in situ* equilibrium electron concentration (Fig. 3c), while lower thickness, higher electron mobility and a deeper work function relative to TiO_2 greatly increases the likelihood of low *in situ* resistances to a level that could pose no fundamental restriction on overall FF.

An interpretation, therefore, of the global trend in certified FF presented in Fig. 4 is an unrecognised mitigation of PSJ resistive losses in the ETL of n–i–p PSC structures, achieved by a transition from TiO_2 to SnO_2. As further evidence, we consider in detail two recent certified efficiencies on small area cells. In late 2020, Jeong *et al.* reported a PCE of 24.6%, on a low-bandgap dual cation perovskite[17] with a remarkable $\sim$300 mV bandgap to open-circuit voltage deficit. The reported voltage is more than 98% of the Shockley–Queisser limit for the given bandgap energy and indicates that non-radiative recombination in the device is extremely low, both in the perovskite bulk and at the interfaces. Optimization of the HTL material maximised PCE primarily through improved FF. Despite this, the certified FF, at 79.7%, is $\sim$10% absolute below the theoretical limit for the measured voltage. If non-radiative recombination cannot explain this deficit, and HTL optimisation reduces the likelihood that the positive terminal is contributing significant FF loss, we are left to propose other sources. The characteristic of the *JV* curve for this cell (Fig. 5) is consistent with significant series resistance (compare with Fig. S1, ESI†). One candidate is Ohmic resistance in the TCO. However, the cell area is approximately 3 × 3 mm^2, which predicts a relative (not absolute) PCE loss of at most 1% in the FTO layer, presuming a sheet resistance of 10 Ω $\square^{-1}$ using the analytical model of Jacobs *et al.*[50] We then consider the negative terminal: the cell was fabricated on an FTO substrate with a spray pyrolysis deposited

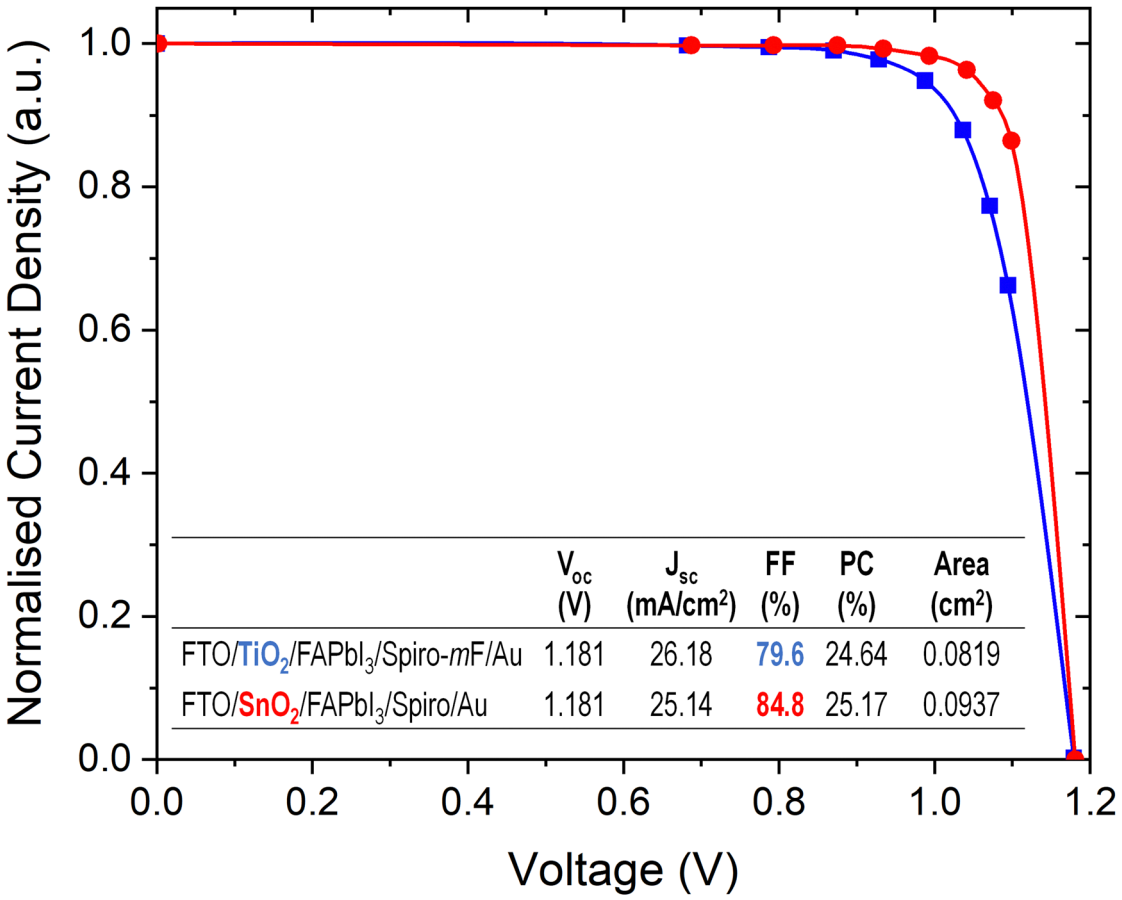

Fig. 5 Certified QSS *JV* data of champion cell from Jeong *et al.*[19] and Yoo *et al.*[18] Data has been digitized and current density normalised for direct comparison. The gradient of the voltage/current relationship between V_{mpp} and V_{oc} ($\sim$1000–1180 mV) is indicative of non-ideal series resistance. The cell of Jeong *et al.* is fabricated on an FTO/TiO_2 substrate, which our analysis suggests may be highly susceptible to power loss due to the TCO/ETL parasitic Schottky junction. By comparison, the certified performance from Yoo *et al.* has achieved a FF 5% absolute greater on a structure based on a FTO/SnO_2 interface.

TiO_2 ETL. As we previously discussed, a low TL dopant density and the predicted range of $\Delta\varphi$ may make this TCO/TL structure susceptible to high ISR. Therefore, a plausible explanation for the unusually low FF relative to the open circuit voltage is the ISR of the TiO_2 layer, with maximum power point resistive voltage losses exacerbated by the high ($\sim$26 mA cm^{-2}) photocurrent.

A comparison to a more recent report by Yoo *et al.*[18] illustrates the magnitude of the ISR power loss that may have occurred in the cells of Jeong *et al.* Yoo *et al.* achieved a certified small area efficiency of 25.2%, in which a key structural change was SnO_2 as the ETL. This cell had a lower photocurrent (25 mA cm^{-2}), and a higher voltage to bandgap energy deficit (389 mV with aperture mask) than Jeong *et al.* yet reported a larger certified FF by 5.2% absolute. The improvement in PCE was thus entirely a result of improved FF. A comparison of the *JV* curves (Fig. 5) shows that this improvement was driven by a reduction in series resistance. The SnO_2 layer—which was optimised to maximise doping density as indicated by UPS data—may therefore be the source of this gain through minimizing ISR. Although Yoo *et al.* ascribed much of the performance enhancement to improvement of the conductivity and conformality of the SnO_2, they did not consider the possibility that PSJ losses were being mitigated. Conversely, Jeong *et al.* may have fabricated a highly efficient device constrained by resistance losses in the ETL, as with control samples in our recent work before the incorporation of TiO_xN_y. If we just consider the *ex situ* conductivity of TiO_2 compared to SnO_2, we do not predict the magnitude of FF increase between these two structures. A straight-forward calculation shows that if a more heavily doped ETL layer ($\geq 10^{17}$ cm^{-3}) were incorporated into the cell structure of Jeong *et al.* to achieve FF on par with the certified value from our recent device ($>$86%), while maintaining the outstanding open-circuit voltage and photocurrent, then PCE would comfortably exceed 26%. This would put perovskite solar cell performance on the same level as the current record in silicon solar cells.[51] TL ISR may therefore be one of the last major unrecognised sources of significant power loss in state-of-the-art PSC structures.

Before we continue to our final line of evidence of ISR losses in the PSCs, we note that Mott–Schottky measurements of TiO_2 have suggested that the ionised dopant density may be on the order of 10^{19} cm^{-3},[2,52] for which our theoretical treatment predicts low ISR. The wide range of reported ionised dopant densities in TiO_2 films may be a function of how the material is fabricated.[53] Notably, we have previously quantified *via* Hall effect measurements an ionised dopant density in ALD-processed TiO_2 in the range of 10^{17}–10^{19} cm^{-3}.[54] This material we incorporated into a 1 cm^2 PSC, which recorded a certified FF of 83.9%.[55] However, beyond direct measurements of TiO_2 $N_D < 10^{16}$ cm^{-3},[1,10,26] there are indirect indications of low ionised dopant density in TiO_2 materials used in PSCs. First is a series of injection-dependent conductivity measurements of TiO_2 performed by Leijtens *et al.*[24] using pulsed laser excitation. These data showed a strong injection-level dependence of conductivity and mobility in TiO_2 across a carrier density range of $\sim 2 \times 10^{16}$–3×10^{17} cm^{-3}, which is inconsistent with an intrinsic dopant density $>10^{19}$ cm^{-3}. This was observed for TiO_2 materials with and without conductivity-enhancing additives.

The second line of evidence of low ionised dopant density in TiO_2 comes from data that also suggest heavy electron depletion and increased ISR in TiO_2 ETLs more generally. These data are cross-sectional contact potential difference (CPD) profiles measured using Kelvin force probe microscopy (KPFM) techniques, which we interpret with the aid of the simulated electric potential profiles of Fig. 3d. CPD measurements capture the spatial distribution of the relative surface potential across a perovskite solar cell with high spatial resolution. Cross section KPFM measurements are technically challenging, but in recent years several groups have published high resolution CPD profiles of complete PSCs.[56–60] These data provide arguably the clearest view into charge distribution in PSCs, and as they capture the potential profile across full devices can reveal the equilibrium distribution of electric charge, and hence the *in situ* space charge within the ETL.

CPD profiles taken from TiO_2/perovskite/spiro PSCs are presented in Fig. 6. These profiles show, in principle, the relative position of the local work function (WF) as the Kelvin probe scans across the cell cross-section, although we must assume that the surface potentials are uniformly indicative of the bulk potential across all layers. By comparing the gradient of the CPD across the TiO_2 layer to the simulated profiles of Fig. 3d, we see that the shallow (quasi-linear) curvature of the profile across the TiO_2 layer in all measurements is consistent with low space charge density, ρ, and hence low N_D (as per Gauss' law, $\nabla^2 V = -\rho/\varepsilon$). Per the simulated electric potential profiles, if the TiO_2 were doped $\geq 10^{18}$ cm^{-3}, we expect to see an exposed space charge density capable of screening the TiO_2 bulk from TCO work function, and hence a bulk potential in the TiO_2 layer that lies closer to the intrinsic work function. As presented, the CPD profiles are instead consistent with the simulated profiles where $N_D < 10^{16}$ cm^{-3}. In addition, the measured profiles are consistent with the space charge region extending the full width of the TiO_2 layer, with implications for bulk non-radiative recombination as discussed in the previous section.

Implications for inverted PSCs

The preceding discussion of n–i–p PSCs has suggested that the PSJ in a TiO_2/TCO layer structure may introduce series resistance that places a fundamental limit on FF, which is circumstantially consistent with historical trends in the certified state-of-the-art performance records in n–i–p PSCs. The obvious comparison is inverted structures, which have repeatedly reported uncertified FF $>$ 84%[61–64] with at least two reports of FF $\geq$ 86%.[63,64] As seen from the perspective of PSJ theory, a key difference between standard and inverted structures is the material that contacts the TCO.

In inverted structures, majority charge carriers can also be depleted from the TCO-adjacent hole transport layer and consequently there is the same dependence on doping density (N_A), $\Delta\varphi$ and thickness to mitigate ISR losses. A common HTL for inverted PSCs with FF $>$ 84% is PEDOT:PSS.[61–63] The doping

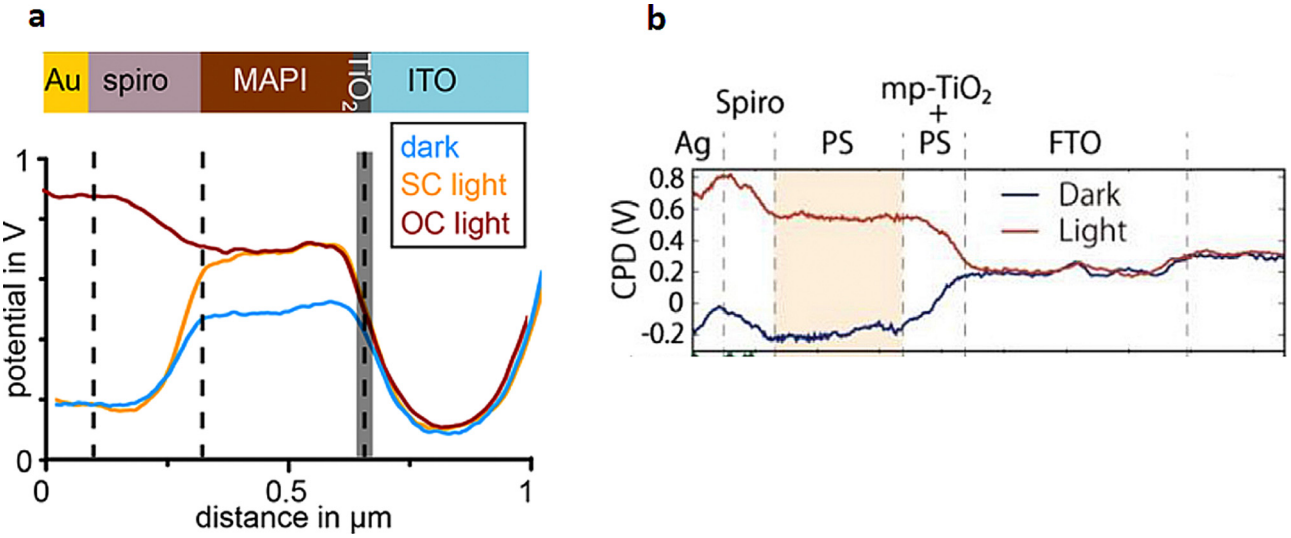

Fig. 6 Contact potential difference profiles take from KPFM measurements of PSC cross sections. In both cases, the electric potential across the TiO_2 layer is consistent with low ionised dopant density and significant depletion from the TiO_2 layer (compare to simulation results of Fig. 3d). (a) Reprinted with permission from Hermes *et al.*, *J. Phys. Chem. Lett.* 2018, 9 (21), 6249–6256. Copyright 2018 American Chemical Society,[58] (b) Reprinted from Cai *et al.*[57]

density, N_A, of PEDOT:PSS typically exceeds $>10^{19}$ cm^{-3} [65] and thickness is approximately 40 nm. The work function of PEDOT:PSS at 4.7–5.4 eV[66] predicts a similar magnitude (although opposite sign) of $\Delta\varphi$ as compared to TiO_2/TCO structures, up to 1.0 eV. Beyond PEDOT:PSS, a notable recent FF of 86.2% is described by Cao *et al.*[64] on a 20 nm NiO_x HTL. Although dopant densities and hence work function vary with preparation method, NiO_x has been reported with doping densities in the range of 10^{16}–10^{19} cm^{-3},[67] and a work-function $\sim$5.0 eV.[68] These HTL materials benefit from reduced thickness and increased ionised dopant density, relative to the TiO_2/TCO structure in n–i–p PSCs. Consequently, inverted cells may have generally achieved higher FF due to widely used HTL materials being both comparatively thin and heavily doped relative to TiO_2, mitigating the ISR.

In this context, it is interesting to note that while inverted cells have achieved FFs greater than n–i–p PSCs, the open circuit voltage and hence PCE is typically lower. For example, Chiang *et al.*[63] reported 86% FF with 1060 mV V_{oc}, Wu *et al.*[62] reported 85% FF and 1030 mV V_{oc}, while the recent 86.2% FF of Cao *et al.*[64] achieved a comparatively modest 1120 mV V_{oc}. In each case, low voltages reduced overall solar cell efficiency. An explanation for the counter-intuitive correlation between FF and open circuit voltage comes from PSJ theory. Firstly, however, we must recognise that FF is a function of both the open circuit voltage and the short circuit current density and the voltage and current density at the maximum power point. In our simulations, we observed that if most non-radiative recombination takes place at a TL interface, then the reduction in maximum power point and open circuit voltage is approximately proportional over a wide range of interface defect concentrations (Fig. 7). In addition, there is minimal influence on the internal quantum efficiency and short circuit current. Consequently, the open circuit and maximum power point voltages fall due to increased recombination, while fill factor remains relatively unchanged.

However, for high FFs to be achieved under low voltages, charge transport resistance across the whole device must be very low. Resistance within the perovskite bulk is expected to be minimal, owing to high perovskite diffusion lengths relative to the absorber thickness, which is suggested by multiple measurements of the electronic quality of perovskite films.[64,69,70] Indeed the 86.2% FF of Cao *et al.* was supported by optimisation of electron and hole mobility in the perovskite layer. In addition, resistance in the transport layers must also be very low. Hence, meaningful ISR would make the combination of low open circuit voltage and high FF extremely difficult to achieve.

To test this notion, we simulated the *JV* characteristics of a PSC in which high TL doping (N_A = 10^{19} cm^{-3}) and high perovskite mobility (μ_e = μ_h = 15 cm^2 V^{-1} s^{-1} as per Cao *et al.*) ensured negligible resistance losses in the cell, most notably the absence of HTL ISR. We varied recombination at the perovskite–HTL interface by adjusting the interfacial recombination-active defect density. As recombination increased and voltage fell, the theoretically achievable FF remained relatively constant at $\gtrsim$87% across a range of V_{oc} from 1000–1200 mV (Fig. 7). The nuances of the injection-dependent recombination dynamics are beyond the scope of our discussion, but these simulations nonetheless illustrate that FF $\gtrsim$ 87% can be achieved in PSCs with voltages as low as 1000 mV, provided no other sources of resistive power loss are present. Therefore, the combination of high FF and low voltage in inverted cells is evidence that these structures are less susceptible to TL ISR losses.

Finally, we must acknowledge that all the calculations in this work have assumed that resistive power losses at the dark side of the cell are very low. In principle, the Schottky junction

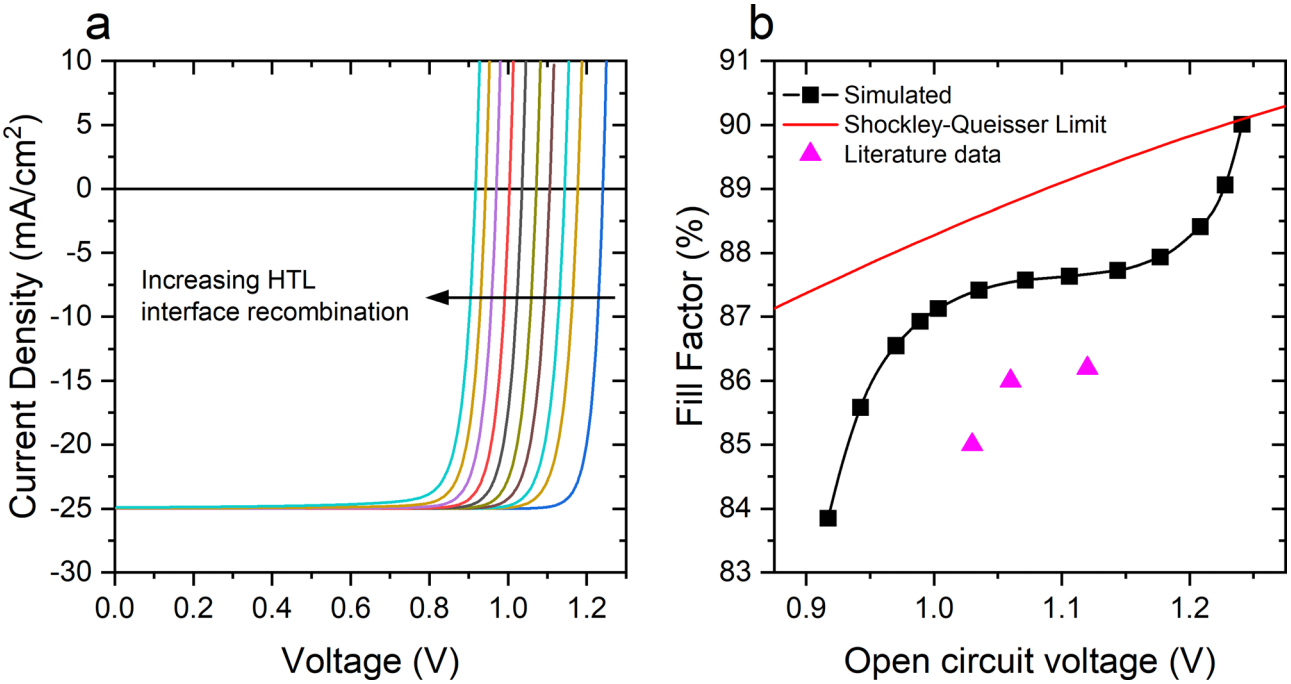

Fig. 7 Simulated FF potential for a PSC in which only non-radiative recombination is the limiting factor on performance (*i.e.* no majority carrier depletion and increased ISR in TL). (a) Simulated *JV* curves *vs.* an increasing density of recombination-active (midgap) defects at the HTL interface. (b) FF as a function of the open-circuit voltage, extracted from the simulated *JV* curves of (a). The FF varies by only 0.5% abs. between open circuit voltages of 1.0–1.2 V due to the approximately proportional reduction in V_{oc} and V_{mpp} as HTL interface defect density increases. The nuance of the relationship between V_{oc} and V_{mpp} is beyond the scope of our discussion here. Instead, these results demonstrate that relatively low voltage is compatible with high FF so long as there is high charge carrier collection efficiency, *e.g.* by avoiding TL series resistance induced by the PSJ. Literature data on V_{oc}-FF in inverted cells are plotted alongside simulated data.[62–64] The relationship between voltage and FF are suggestive of very low resistance losses, including PSJ losses in these inverted cell architectures.

that can lead to majority carrier depletion at the TL–TCO interface can also occur at the metalized side of the PSC. Referring to the FF gains from the incorporation of TiO_xN_y, cell performance suggests that in this structure resistance losses introduced by the HTL must be relatively small. It is possible that the practical $\Delta\varphi$ of the TL–Au interface is negligible, potentially a consequence of Fermi-level pinning as is widely observed for metal contacts.[36] Evidence for low $\Delta\varphi$ may be observed in the CPD profile of Fig. 6a, which shows flat band conditions across the interface between SPIRO:OMeTAD HTL and the Au electrode.

Recommendations for future characterisation

Our theoretical treatment, as with all numerical perovskite solar cell simulations to date, has assumed idealised alignment of energy bands in the cell.[71] However, interface states that are unique to the combination of materials can lead to Fermi level pinning, which result in a built-in potential that differs from idealised predictions using data measured on films in isolation.[36] Furthermore, other effects such as ion migration into the transport layers,[72,73] interfacial dipoles[74] and surface morphology[55] can influence the energy landscape of the junction. Therefore, even with accurate quantification of the band structure of the TL, reliable predictions of the TCO/TL interface properties will be challenging *a priori*.

Nonetheless, our simulations have shown that the predicted range of work function differences between the TL and TCO makes space charge in the TL highly probable, with uncertainty existing only in the magnitude of the majority carrier depletion and the corresponding increase in ISR. Therefore, in characterising TL materials intended for the TL/TCO interface, we recommend routinely quantifying properties that minimise the likelihood of significant ISR for any eventual potential difference between the TCO and the TL, in addition to direct quantification of the current–voltage properties of the TCO/TL junction itself. For the TL, dopant density and majority carrier mobility are two critical parameters as they determine the susceptibility of the material to an *in situ* reduction in conductivity at any given $\Delta\varphi$. As the method of fabrication and the inclusion of additives can have a significant influence of dopant density, this may require measurements taken in-house that reflect the specific composition employed, as opposed to relying on literature data.

The work function difference, $\Delta\varphi$, also plays an important role. Consequently, it may be necessary to quantify the current–voltage properties of the TL/TCO interface using dedicated test structures. In Fig. S6 (ESI†) we plot simulated current–voltage curves for a TL/TCO structure, where each interface is contacted *via* an Ohmic electrode. These simulations demonstrate the mild rectification predicted for conditions in which $\Delta\varphi$ falls within the sub s-shape range we previously identified,

appearing as a resistance to current flow that is asymmetric with polarity across the TL/TCO interface. To reiterate, where $\Delta\varphi$ is sufficiently large such that the TL/TCO is strongly rectifying against current flow from the cell—a result of a large built-in potential in the junction—the *JV* characteristics of the cell will exhibit an s-shape that clearly identifies a structural problem.

Conclusion

Achieving maximum efficiency in single junction or tandem perovskite solar cells will require a clear view of all possible sources of power loss. In this work, we considered the impact of the Schottky-type heterojunction formed between the TCO and the adjacent transport layer (TL) on the *in situ* conductivity of the TL. Using numerical ionic–electronic device modelling, we illustrated how majority carrier depletion of the transport layer can result in increased series resistance that would be unexpected based on an *ex situ* quantification of transport layer conductivity. In addition, where the depletion region extends the full width of the TL, the TCO work function can increase non-radiative recombination rates within the perovskite itself, reducing cell voltage. Critical is the observation that the resistive power loss due to this junction does not need to have the characteristic ''s-shape'' that is symptomatic of high energy barriers to majority carrier flow at the TL–TCO interface. While the intrinsic conductivity of a transport layer is clearly still an important factor, it is ultimately the conductivity of the transport layer once in electrostatic equilibrium with the TCO that determines the achievable fill factor of a perovskite solar cell.

Factors that minimise the width of the depletion region in the TL will reduce majority carrier depletion and *in situ* resistance, namely an increase in TL doping and a decrease in the work function difference between the two layers. In addition, significant reductions in thickness to <20 nm will reduce overall resistance in otherwise heavily depleted layers but come with practical challenges that may instead favour the use of heavily doped or high mobility materials. As a case study, we considered the widely used electrode structure fabricated from TCO/TiO_2 layers. Hall effect measurements and CPD profiles of PSCs taken from literature suggest that TiO_2 can have intrinsically low ionised dopant densities $<10^{16}$ cm^{-3}. Thus, majority carrier depletion can reduce *in situ* conductivity and plausibly restrict maximum FF to the low 80 s in cells with ETL films of typical 50 nm thickness. This prediction is circumstantially consistent with the years-long plateau of *circa* 80% in certified FF on TiO_2 PSCs, with the highest certified FF of non-ALD TiO_2-based PSCs having only recently reached 81.8%.[19] A step change in certified FFs in record n–i–p PSCs coincided with the transition to SnO_2[18] and TiO_xN_y[1] ETLs. From the perspective of the PSJ, SnO_2 and TiO_xN_y benefit from high ionised dopant densities, while SnO_2 exhibits a higher majority carrier mobility and a deeper work function relative to TiO_2. Going forward, the continued use of TiO_2 will likely require significantly thinner layers <20 nm that do not compromise uniform coverage or exploration of deposition methods that can reliably produce high ionised dopant densities, as may be the case for ALD TiO_2.[54] By considering recent records in PSC performance, we illustrate how mitigation of TCO-induced ETL depletion could increase PCEs above 26%.

In the context of inverted PSCs, we suggest that repeated reports of FFs >84%, including two reports >86%, may in part be the result of reduced susceptibility of common HTL materials to TCO-induced *in situ* resistance. A major factor distinguishing inverted cell structures is the material that contacts the TCO, with high performance HTLs such as PEDOT:PSS and NiO_x mitigating *in situ* resistance through generally higher ionised dopant densities and thinner layers. This comparison further emphasizes TiO_2 as a weak link in PSC design.

We conclude with three important points. Firstly, the magnitude of the power loss introduced by the TCO/TL junction is dependent on material properties—such as the ionised dopant density of the TL—that are not routinely quantified. This work has demonstrated the possible extent of these losses based on a plausible range of material parameters. But given the potential for significant resistance in non-ideal TL/TCO structures, we suggest routine characterisation of TL dopant density, majority carrier mobility and the current-voltage properties of the resultant TL/TCO structure. Secondly, for device modelling to be representative of the electrostatics of complete PSCs, the TCO must be incorporated into PSC theory. Finally, mitigation of *in situ* depletion of the TCO-adjacent transport layer is necessary but not sufficient to achieve high PCEs. All other factors of the cell must be highly performant. Our argument is that the TL/TCO heterojunction can introduce significant and often unrecognised sources of power loss in state-of-the-art PSCs, constraining otherwise high-performance cells.

Author contributions

D. W. constructed and performed numerical simulations and prepared manuscript. JP performed key data analysis, experimental work and contributed to manuscript. K. W., K. R. C. and T. W. all contributed to theoretical discussion and manuscript preparation.

Conflicts of interest

There are no conflicts to declare.

Acknowledgements

This work was supported by the Australian Government through the Australian Renewable Energy Agency and the Australian Research Council. Responsibility for the views, information or advice expressed herein is not accepted by the Australian Government. D. W. and J. P. acknowledge the financial support of Postdoc Fellowships from the Australian Centre for Advanced Photovoltaics. T. P. W. is the recipient of an Australian Research Council Future Fellowship (project

number FT180100302) funded by the Australian Government. This research/project was undertaken with the assistance of resources and services from the National Computational Infrastructure (NCI), which is supported by the Australian Government.

Notes and references

1 J. Peng, F. Kremer, D. Walter, Y. Wu, Y. Ji, J. Xiang, W. Liu, T. Duong, H. Shen, T. Lu, F. Brink, D. Zhong, L. Li, O. Lee Cheong Lem, Y. Liu, K. J. Weber, T. P. White and K. R. Catchpole, *Nature*, 2022, **601**, 573–578.
2 K. Wojciechowski, S. D. Stranks, A. Abate, G. Sadoughi, A. Sadhanala, N. Kopidakis, G. Rumbles, C.-Z. Li, R. H. Friend, A. K.-Y. Jen and H. J. Snaith, *ACS Nano*, 2014, **8**, 12701–12709.
3 H. J. Snaith and M. Grätzel, *Adv. Mater.*, 2006, **18**, 1910–1914.
4 M. Bivour, C. Reichel, M. Hermle and S. W. Glunz, *Sol. Energy Mater. Sol. Cells*, 2012, **106**, 11–16.
5 L. Zhao, C. L. Zhou, H. L. Li, H. W. Diao and W. J. Wang, *Phys. Status Solidi A*, 2008, **205**, 1215–1221.
6 G. Kron, T. Egerter, J. H. Werner and U. Rau, *J. Phys. Chem. B*, 2003, **107**, 3556–3564.
7 H. Zhou, Q. Chen, G. Li, S. Luo, T. Song, H.-S. Duan, Z. Hong, J. You, Y. Liu and Y. Yang, *Science*, 2014, **345**, 542–546.
8 K. Wojciechowski, M. Saliba, T. Leijtens, A. Abate and H. J. Snaith, *Energy Environ. Sci.*, 2014, **7**, 1142–1147.
9 W. Chen, Y. Wu, Y. Yue, J. Liu, W. Zhang, X. Yang, H. Chen, E. Bi, I. Ashraful, M. Grätzel and L. Han, *Science*, 2015, **350**, 944–948.
10 X. Yin, Y. Guo, Z. Xue, P. Xu, M. He and B. Liu, *Nano Res.*, 2015, **8**, 1997–2003.
11 T. Wu, C. Zhen, H. Zhu, J. Wu, C. Jia, L. Wang, G. Liu, N.-G. Park and H.-M. Cheng, *ACS Appl. Mater. Interfaces*, 2019, **11**, 19638–19646.
12 T. S. Sherkar, C. Momblona, L. Gil-Escrig, H. J. Bolink and L. J. A. Koster, *Adv. Energy Mater.*, 2017, **7**, 1602432.
13 S. van Reenen, M. Kemerink and H. J. Snaith, *J. Phys. Chem. Lett.*, 2015, **6**, 3808–3814.
14 G. Richardson, S. E. J. O'Kane, R. G. Niemann, T. A. Peltola, J. M. Foster, P. J. Cameron and A. B. Walker, *Energy Environ. Sci.*, 2016, **9**, 1476–1485.
15 D. A. Jacobs, H. Shen, F. Pfeffer, J. Peng, T. P. White, F. J. Beck and K. R. Catchpole, *J. Appl. Phys.*, 2018, **124**, 225702.
16 N. E. Courtier, J. M. Cave, J. M. Foster, A. B. Walker and G. Richardson, *Energy Environ. Sci.*, 2019, **12**, 396–409.
17 M. Jeong, I. W. Choi, E. M. Go, Y. Cho, M. Kim, B. Lee, S. Jeong, Y. Jo, H. W. Choi, J. Lee, J.-H. Bae, S. K. Kwak, D. S. Kim and C. Yang, *Science*, 2020, **369**, 1615–1620.
18 J. J. Yoo, G. Seo, M. R. Chua, T. G. Park, Y. Lu, F. Rotermund, Y.-K. Kim, C. S. Moon, N. J. Jeon, J.-P. Correa-Baena, V. Bulović, S. S. Shin, M. G. Bawendi and J. Seo, *Nature*, 2021, **590**, 587–593.
19 J. Jeong, M. Kim, J. Seo, H. Lu, P. Ahlawat, A. Mishra, Y. Yang, M. A. Hope, F. T. Eickemeyer, M. Kim, Y. J. Yoon, I. W. Choi, B. P. Darwich, S. J. Choi, Y. Jo, J. H. Lee, B. Walker, S. M. Zakeeruddin, L. Emsley, U. Rothlisberger, A. Hagfeldt, D. S. Kim, M. Grätzel and J. Y. Kim, *Nature*, 2021, **592**, 381–385.
20 D. Walter, A. Fell, Y. Wu, T. Duong, C. Barugkin, N. Wu, T. White and K. Weber, *J. Phys. Chem. C*, 2018, **122**, 11270–11281.
21 N. Mozaffari, D. Walter, T. P. White, A. D. Bui, G. D. Tabi, K. Weber and K. R. Catchpole, *Solar RRL*, 2022, **6**, 2200355.
22 B.-X. Chen, H.-S. Rao, W.-G. Li, Y.-F. Xu, H.-Y. Chen, D.-B. Kuang and C.-Y. Su, *J. Mater. Chem. A*, 2016, **4**, 5647–5653.
23 J. H. Heo, H. J. Han, D. Kim, T. K. Ahn and S. H. Im, *Energy Environ. Sci.*, 2015, **8**, 1602–1608.
24 T. Leijtens, J. Lim, J. Teuscher, T. Park and H. J. Snaith, *Adv. Mater.*, 2013, **25**, 3227–3233.
25 C. Liang, P. Li, Y. Zhang, H. Gu, Q. Cai, X. Liu, J. Wang, H. Wen and G. Shao, *J. Power Sources*, 2017, **372**, 235–244.
26 J. Peng, T. Duong, X. Zhou, H. Shen, Y. Wu, H. K. Mulmudi, Y. Wan, D. Zhong, J. Li, T. Tsuzuki, K. J. Weber, K. R. Catchpole and T. P. White, *Adv. Energy Mater.*, 2017, **7**, 1601768.
27 C. Wang, C. Xiao, Y. Yu, D. Zhao, R. A. Awni, C. R. Grice, K. Ghimire, I. Constantinou, W. Liao, A. J. Cimaroli, P. Liu, J. Chen, N. J. Podraza, C.-S. Jiang, M. M. Al-Jassim, X. Zhao and Y. Yan, *Adv. Energy Mater.*, 2017, **7**, 1700414.
28 J. Peng, F. Kremer, D. Walter, Y. Wu, Y. Ji, W. Liu, J. Xiang, H. Shen, T. Lu, F. Brink, D. Zhong, Y. Liu, K. J. Weber, T. P. White and K. R. Catchpole.
29 R. D. Chavan, P. Yadav, A. Nimbalkar, S. P. Bhoite, P. N. Bhosale and C. Kook Hong, *Sol. Energy*, 2019, **186**, 156–165.
30 X.-X. Gao, Q.-Q. Ge, D.-J. Xue, J. Ding, J.-Y. Ma, Y.-X. Chen, B. Zhang, Y. Feng, L.-J. Wan and J.-S. Hu, *Nanoscale*, 2016, **8**, 16881–16885.
31 M. Kim, I. Choi, S. J. Choi, J. W. Song, S.-I. Mo, J.-H. An, Y. Jo, S. Ahn, S. K. Ahn, G.-H. Kim and D. S. Kim, *Joule*, 2021, **5**, 659–672.
32 S. Lee, S. Kim, S. Shin, Z. Jin and Y.-S. Min, *J. Ind. Eng. Chem.*, 2018, **58**, 328–333.
33 L. Xiong, Y. Guo, J. Wen, H. Liu, G. Yang, P. Qin and G. Fang, *Adv. Funct. Mater.*, 2018, **28**, 1802757.
34 A. Andersson, N. Johansson, P. Bröms, N. Yu, D. Lupo and W. R. Salaneck, *Adv. Mater.*, 1998, **10**, 859–863.
35 N. Balasubramanian and A. Subrahmanyam, *J. Electrochem. Soc.*, 1991, **138**, 322.
36 R. T. Tung, *Appl. Phys. Rev.*, 2014, **1**, 011304.
37 E. Aydin, M. De Bastiani, X. Yang, M. Sajjad, F. Aljamaan, Y. Smirnov, M. N. Hedhili, W. Liu, T. G. Allen, L. Xu, E. Van Kerschaver, M. Morales-Masis, U. Schwingenschlögl and S. De Wolf, *Adv. Funct. Mater.*, 2019, **29**, 1901741.
38 Q. Jiang, X. Zhang and J. You, *Small*, 2018, **14**, 1801154.

39 K. C. Fong, T. C. Kho, W. Liang, T. K. Chong, M. Ernst, D. Walter, M. Stocks, E. Franklin, K. McIntosh and A. Blakers, *Sol. Energy Mater. Sol. Cells*, 2018, **186**, 236–242.
40 A. Kogo, Y. Sanehira, Y. Numata, M. Ikegami and T. Miyasaka, *ACS Appl. Mater. Interfaces*, 2018, **10**, 2224–2229.
41 H. Tang, K. Prasad, R. Sanjinès, P. E. Schmid and F. Lévy, *J. Appl. Phys.*, 1994, **75**, 2042–2047.
42 C. Altinkaya, E. Aydin, E. Ugur, F. H. Isikgor, A. S. Subbiah, M. De Bastiani, J. Liu, A. Babayigit, T. G. Allen, F. Laquai, A. Yildiz and S. De Wolf, *Adv. Mater.*, 2021, **33**, 2005504.
43 M. A. Green, E. D. Dunlop, J. Hohl-Ebinger, M. Yoshita, N. Kopidakis and X. Hao, *Prog. Photovoltaics Res. Appl.*, 2021, **29**, 657–667.
44 H. Liu, J. Tang, I. J. Kramer, R. Debnath, G. I. Koleilat, X. Wang, A. Fisher, R. Li, L. Brzozowski, L. Levina and E. H. Sargent, *Adv. Mater.*, 2011, **23**, 3832–3837.
45 L. Kavan, L. Steier and M. Grätzel, *J. Phys. Chem. C*, 2017, **121**, 342–350.
46 B. Roose, C. M. Johansen, K. Dupraz, T. Jaouen, P. Aebi, U. Steiner and A. Abate, *J. Mater. Chem. A*, 2018, **6**, 1850–1857.
47 Q. Jiang, L. Zhang, H. Wang, X. Yang, J. Meng, H. Liu, Z. Yin, J. Wu, X. Zhang and J. You, *Nat. Energy*, 2016, **2**, 1–7.
48 H. J. Snaith and C. Ducati, *Nano Lett.*, 2010, **10**, 1259–1265.
49 W. Ke, D. Zhao, A. J. Cimaroli, C. R. Grice, P. Qin, Q. Liu, L. Xiong, Y. Yan and G. Fang, *J. Mater. Chem. A*, 2015, **3**, 24163–24168.
50 D. A. Jacobs, K. R. Catchpole, F. J. Beck and T. P. White, *J. Mater. Chem. A*, 2016, **4**, 4490–4496.
51 K. Yoshikawa, H. Kawasaki, W. Yoshida, T. Irie, K. Konishi, K. Nakano, T. Uto, D. Adachi, M. Kanematsu, H. Uzu and K. Yamamoto, *Nat. Energy*, 2017, **2**, 17032.
52 L. Kavan and M. Grätzel, *Electrochim. Acta*, 1995, **40**, 643–652.
53 B. Roose, S. Pathak and U. Steiner, *Chem. Soc. Rev.*, 2015, **44**, 8326–8349.
54 H. Shen, S. T. Omelchenko, D. A. Jacobs, S. Yalamanchili, Y. Wan, D. Yan, P. Phang, T. Duong, Y. Wu, Y. Yin, C. Samundsett, J. Peng, N. Wu, T. P. White, G. G. Andersson, N. S. Lewis and K. R. Catchpole, *Sci. Adv.*, 2018, **4**, eaau9711.
55 J. Peng, D. Walter, Y. Ren, M. Tebyetekerwa, Y. Wu, T. Duong, Q. Lin, J. Li, T. Lu, M. A. Mahmud, O. L. C. Lem, S. Zhao, W. Liu, Y. Liu, H. Shen, L. Li, F. Kremer, H. T. Nguyen, D.-Y. Choi, K. J. Weber, K. R. Catchpole and T. P. White, *Science*, 2021, **371**, 390–395.
56 V. W. Bergmann, Y. Guo, H. Tanaka, I. M. Hermes, D. Li, A. Klasen, S. A. Bretschneider, E. Nakamura, R. Berger and S. A. L. Weber, *ACS Appl. Mater. Interfaces*, 2016, **8**, 19402–19409.
57 M. Cai, N. Ishida, X. Li, X. Yang, T. Noda, Y. Wu, F. Xie, H. Naito, D. Fujita and L. Han, *Joule*, 2018, **2**, 296–306.
58 I. M. Hermes, Y. Hou, V. W. Bergmann, C. J. Brabec and S. A. L. Weber, *J. Phys. Chem. Lett.*, 2018, **9**, 6249–6256.
59 C.-S. Jiang, M. Yang, Y. Zhou, B. To, S. U. Nanayakkara, J. M. Luther, W. Zhou, J. J. Berry, J. van de Lagemaat, N. P. Padture, K. Zhu and M. M. Al-Jassim, *Nat. Commun.*, 2015, **6**, 8397.
60 S. A. L. Weber, I. M. Hermes, S.-H. Turren-Cruz, C. Gort, V. W. Bergmann, L. Gilson, A. Hagfeldt, M. Graetzel, W. Tress and R. Berger, *Energy Environ. Sci.*, 2018, **11**, 2404–2413.
61 K. Wang, C. Liu, P. Du, J. Zheng and X. Gong, *Energy Environ. Sci.*, 2015, **8**, 1245–1255.
62 C.-G. Wu, C.-H. Chiang, Z.-L. Tseng, M. K. Nazeeruddin, A. Hagfeldt and M. Grätzel, *Energy Environ. Sci.*, 2015, **8**, 2725–2733.
63 C.-H. Chiang and C.-G. Wu, *ACS Nano*, 2018, **12**, 10355–10364.
64 Q. Cao, Y. Li, H. Zhang, J. Yang, J. Han, T. Xu, S. Wang, Z. Wang, B. Gao, J. Zhao, X. Li, X. Ma, S. M. Zakeeruddin, W. E. I. Sha, X. Li and M. Grätzel, *Sci. Adv.*, 2021, **7**, eabg0633.
65 E. Jin Bae, Y. Hun Kang, K.-S. Jang and S. Yun Cho, *Sci. Rep.*, 2016, **6**, 18805.
66 A. M. Nardes, M. Kemerink, M. M. de Kok, E. Vinken, K. Maturova and R. A. J. Janssen, *Org. Electron.*, 2008, **9**, 727–734.
67 H. Sun, S.-C. Chen, P.-J. Chen, S.-L. Ou, C.-Y. Liu and Y.-Q. Xin, *Ceram. Int.*, 2018, **44**, 3291–3296.
68 M. D. Irwin, D. B. Buchholz, A. W. Hains, R. P. H. Chang and T. J. Marks, *Proc. Natl. Acad. Sci. U. S. A.*, 2008, **105**, 2783–2787.
69 S. D. Stranks, G. E. Eperon, G. Grancini, C. Menelaou, M. J. P. Alcocer, T. Leijtens, L. M. Herz, A. Petrozza and H. J. Snaith, *Science*, 2013, **342**, 341–344.
70 I. L. Braly, D. W. deQuilettes, L. M. Pazos-Outón, S. Burke, M. E. Ziffer, D. S. Ginger and H. W. Hillhouse, *Nat. Photonics*, 2018, **12**, 355.
71 R. L. Anderson, *IBM J. Res. Dev.*, 1960, **4**, 283–287.
72 Z. Li, C. Xiao, Y. Yang, S. P. Harvey, D. Hoe Kim, J. A. Christians, M. Yang, P. Schulz, S. U. Nanayakkara, C.-S. Jiang, J. M. Luther, J. J. Berry, M. C. Beard, M. M. Al-Jassim and K. Zhu, *Energy Environ. Sci.*, 2017, **10**, 1234–1242.
73 R. A. Z. Razera, D. A. Jacobs, F. Fu, P. Fiala, M. Dussouillez, F. Sahli, T. C. J. Yang, L. Ding, A. Walter, A. F. Feil, H. I. Boudinov, S. Nicolay, C. Ballif and Q. Jeangros, *J. Mater. Chem. A*, 2019, **8**, 242–250.
74 Q. Chen, C. Wang, Y. Li and L. Chen, *J. Am. Chem. Soc.*, 2020, **142**, 18281–18292.
75 J. Burschka, N. Pellet, S.-J. Moon, R. Humphry-Baker, P. Gao, M. K. Nazeeruddin and M. Grätzel, *Nature*, 2013, **499**, 316–319.
76 W. S. Yang, J. H. Noh, N. J. Jeon, Y. C. Kim, S. Ryu, J. Seo and S. I. Seok, *Science*, 2015, **348**, 1234–1237.
77 W. S. Yang, B.-W. Park, E. H. Jung, N. J. Jeon, Y. C. Kim, D. U. Lee, S. S. Shin, J. Seo, E. K. Kim, J. H. Noh and S. I. Seok, *Science*, 2017, **356**, 1376–1379.
78 E. H. Jung, N. J. Jeon, E. Y. Park, C. S. Moon, T. J. Shin, T.-Y. Yang, J. H. Noh and J. Seo, *Nature*, 2019, **567**, 511–515.
79 Q. Jiang, Z. Chu, P. Wang, X. Yang, H. Liu, Y. Wang, Z. Yin, J. Wu, X. Zhang and J. You, *Adv. Mater.*, 2017, **29**, 1703852.

